

A Highly Overmoded Structure for Hundred-Kilowatt-Class *Ka*-Band Extended Interaction Klystron

Yifan Zu, Xuesong Yuan¹, Xiaotao Xu, Hailong Li¹, *Member, IEEE*, Qingyun Chen¹, Matthew Thomas Cole², *Senior Member, IEEE*, Lin Meng, and Yang Yan

Abstract—Here, we report on the development of highly overmoded structure for a millimeter-wave (MMW) extended interaction klystron (EIK). To enhance electron beam loading, a new method for designing an oversized beam tunnel in a large cavity by concentrating the axial field is demonstrated. The transmission and oscillation characteristics of the interaction circuit operating in the quasi-TM₀₄ mode are tested by the developed mode conversion circuit. Results suggest that a five-cavity EIK based on this highly overmoded structure can achieve an output power of 289 kW at 32.92 GHz with a saturated gain of 51.6 dB by injecting a 3.3-mm-diameter electron beam with a current of 18 A. The output power exceeds 100 kW at a bandwidth of 100 MHz.

Index Terms—*Ka*-band, Extended interaction klystron (EIK), highly overmoded structure, vacuum electronics.

I. INTRODUCTION

DEMAND for mobile, high-power electromagnetic radiation sources suitable for millimeter-wave (MMW) applications is booming due to their potential applications in concealed weapon or threat detection, fine spatial resolution radar, and high data rate communications [1], [2], [3], [4]. As one of the most competitive candidates for high power generation in the family of vacuum electronic devices, extended interaction klystron (EIK) has shorter circuit length than traveling-wave tube (TWT) and lower magnetic field requirement than gyrotron [5], [6], [7], [8], [9]. A *Ka*-band

Manuscript received 17 July 2023; accepted 10 August 2023. This work was supported in part by the National Key Research and Development Program of China under Grant 2019YFA0210202, in part by the Fundamental Research Funds for the Central Universities under Grant ZYGX2019J012, and in part by the National Natural Science Foundation of China under Grant 61771096. The review of this article was arranged by Editor S. Prasad. (*Corresponding authors: Xuesong Yuan; Hailong Li.*)

Yifan Zu, Xuesong Yuan, Xiaotao Xu, Hailong Li, Qingyun Chen, Lin Meng, and Yang Yan are with the Terahertz Science and Technology Key Laboratory of Sichuan Province, School of Electronic Science and Engineering, University of Electronic Science and Technology of China, Chengdu 611731, China (e-mail: yuanxs@uestc.edu.cn; lihailong@uestc.edu.cn).

Matthew Thomas Cole is with the Department of Electronic and Electrical Engineering, University of Bath, BA2 7AY Bath, U.K. (e-mail: m.t.cole@bath.ac.uk).

Color versions of one or more figures in this article are available at <https://doi.org/10.1109/TED.2023.3305952>.

Digital Object Identifier 10.1109/TED.2023.3305952

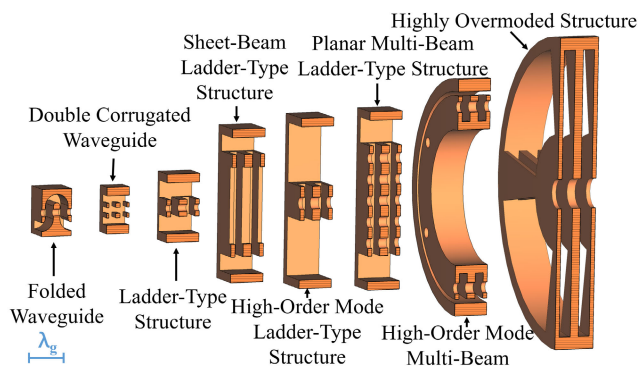


Fig. 1. Schematic of various periodic high-frequency (HF) structures for linear beam devices at the same frequency band.

EIK prototype tube developed by the Institute of Electronics, Chinese Academy of Sciences, has been tested to achieve an output power of 20 kW in the 60-MHz bandwidth [10]. However, the compact size of this ladder-type structure requires in principle that the electron beam must have tiny transverse dimensions and potentially very high current densities to maintain sufficiently high gain and power [11]. To a significant extent, the limits on this compact structure performance are a consequence on the challenges of generating high current, small diameter, precisely aligned electron beams.

To improve power handling capabilities, insights gained using overmoded structures in fast-wave device development can be extended to linear beam devices [12]. The power limitation imposed by cross-sectional dimensions that shrink with wavelength can be overcome by using cavities and waveguides that are much larger than the wavelength in the transverse dimension due to operation in higher order modes.

In this article, a highly overmoded interaction circuit is proposed. The operation mechanism of the quasi-TM₀₄ in this circuit is established. Due to the realization of the method of concentrating the axial field energy along the source's central axis within a large cavity, an oversized beam tunnel that can support efficient energy conversion between the electron beam and the high frequency (HF) field is designed. As shown in Fig. 1, this highly overmoded structure has

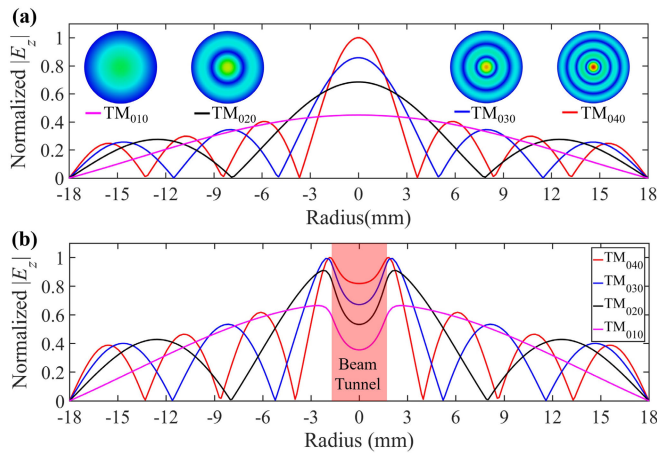


Fig. 2. (a) Normalized $|E_z|$ -field amplitude distribution along the radial direction. Insets: electric field distribution at cross section of TM_{010} , TM_{020} , TM_{030} , and TM_{040} modes. (b) Normalized $|E_z|$ -field amplitude distribution across the cross section of the same cylindrical cavity resonator with beam tunnel.

a far larger electron beam loading area than conventional structures [13], [14], [15], [16]. Even compared to sheet beam and multibeam, its single tunnel can still support an intense electron beam with a high total current without the need for complex electron optical system and focusing system [17], [18]. Due to the Bessel function cross-sectional field strength distribution, the higher the order of the TM mode, the stronger the E_z -field strength around the central axis, and the greater the characteristic impedance, as shown in Fig. 2, which is extremely beneficial to suppress the generation of low-order modes [19]. Based on this quasi- TM_{04} mode structure, a five-cavity Ka -band EIK with hundred-kilowatt-class output power is thus demonstrated.

II. CIRCUIT DESIGN

A. Four-Coupling-Hole Disk Periodic Structure

Compared with the commonly used fundamental mode, the most significant feature of the higher order mode is that it can support a physically larger HF structure for a given frequency [20]. Furthermore, as shown in Fig. 2, the concentration of the axial electric field not only improves the beam-wave interaction but also makes it possible to expand the diameter of the beam tunnel. All of these efforts are justified because the apparent increase in the transverse dimension of the HF structures relative to the wavelength allows the application of denser electron beams, which will translate into further improvements in generation power and microwave pulse duration. After preliminary empirical analysis of the higher order mode field of the cylindrical cavity resonator, the TM_{04} -based mode is selected. Here, a highly overmoded resonant slow wave structure (RSWS) that operates stably in the quasi- TM_{04} mode is presented. Fig. 3(a) and (b) shows the E_z -field distribution at the cross section of a single interaction gap. Fig. 4 shows the manufactured parts to assemble the highly overmoded RSWS and the experimental measurement setup.

The core technology for forming the designed RSWS operating in the quasi- TM_{04} mode with a large-aperture beam

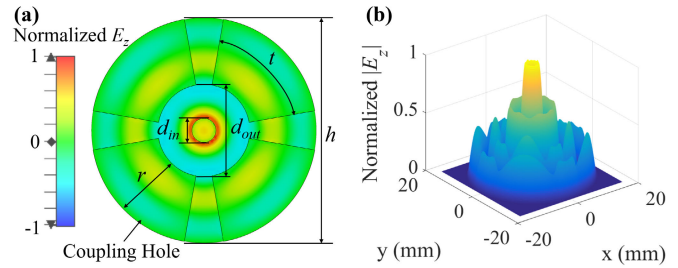


Fig. 3. (a) E_z -field distribution. (b) $|E_z|$ -field contour plot of the quasi- TM_{04} mode at $z = 0$ plane.

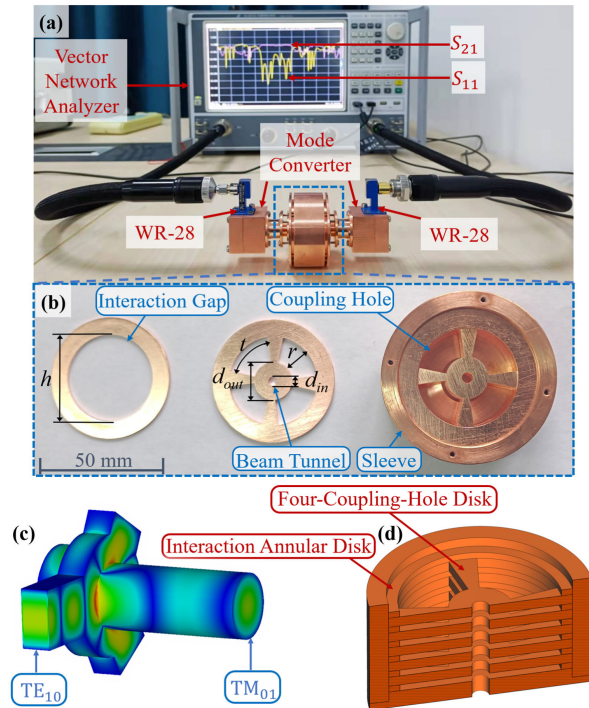


Fig. 4. (a) Experimental setup for measuring the transmission properties of the RSWS. (b) Photograph of the manufactured RSWS components (scale bar: 50 mm). (c) Electric field distribution in the mode converter. (d) Schematic of the RSWS cross section composed of multiple disks.

tunnel is the introduction of a periodically superimposed central disk. Since the central disk cannot be suspended in the cavity, the coupling holes are formed between the supporting plates connected with the inner wall of the cavity. This RSWS is a periodic structure composed of a plurality of four-coupling-hole disks and interaction annular disks and then packed into a sleeve, as shown in Fig. 4(b). The structural parameters of the four-coupling-hole disk and the interaction annular disk are given as follows: the diameter of the entire cavity h is 34 mm, the diameter of the beam tunnel d_{in} is 3.6 mm, the outer diameter of the center disk d_{out} is 14 mm, the radius of the coupling hole r is 10 mm, and the angular width of the coupling hole t is 70° . Fig. 4(d) shows the cross-sectional view after loading multiple four-coupling-hole disks and interaction annular disks sequentially.

The transmission and oscillation characteristics of the circuit are investigated using mode converters from the TE_{10} mode of the rectangular waveguide to the TM_{01} mode of the circular

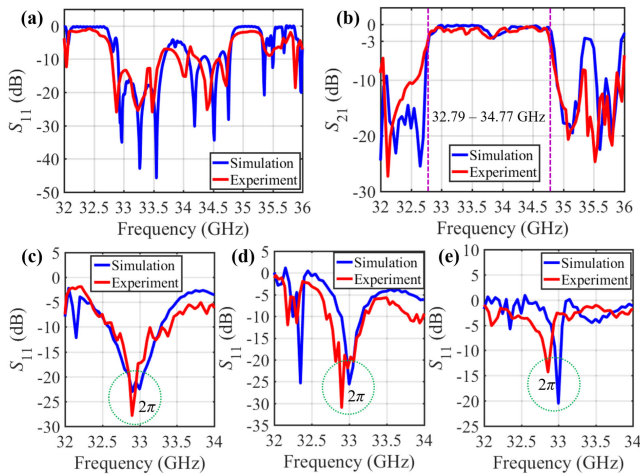


Fig. 5. Comparison of experimental and simulation results for seven gaps: (a) S_{11} and (b) S_{21} , (c) two-gap S_{11} , (d) three-gap S_{11} , and (e) four-gap S_{11} of the RSWS.

waveguide [21]. The mode converter consists of a circular waveguide that can be connected to the RSWS, and an intermediate circular coupling cavity, a circular waveguide short-circuit plane, and three rectangular waveguides placed at 120° at the intersection of the coupled section. The mode converter has two ports: a circular waveguide (port 2) connected to the interaction circuit and an elongated rectangular waveguide (port 1). Fig. 4(c) shows the electric field distribution in a single-mode converter when TE_{10} is fed from port 1 and TM_{01} is output from port 2. The rectangular waveguides are standard commercial WR-28 waveguides (7.11×3.56 mm).

Fig. 5 shows the comparison between the simulated and experimental S -parameters for this highly overmoded RSWS. The multigap cavity of the extended interaction device is a resonant slow wave circuit with short circuit at both ends of the slow wave line. When the number of gaps is small, the resonant cavity characteristics dominate. When the number of gaps increases, the characteristics of the resonant structure will also gradually attach the slow wave line characteristics. In the case of seven gaps, the transmission characteristics of the RSWS are obtained, as shown in Fig. 5(b). Our experimental results demonstrate that the circuit has a transmission coefficient S_{21} of ≥ -3 dB in the range of 32.79–34.77 GHz. As shown in Fig. 5(c)–(e), respectively, the oscillatory characteristics of the 2π mode of the RSWS are obtained in the cases of two, three, and four gaps.

Based on the RSWS, a *Ka*-band EIK consisting of an input cavity, three middle cavities, and an output cavity has been designed, as shown in Fig. 6. The HF characteristics of the highly overmoded structure are calculated using the commercially available 3-D electromagnetic analysis software (CST). Table I lists the physical parameters of each cavity, where f is the resonant frequency, p is the period length, $M^2(R/Q)$ is the effective characteristic impedance for evaluating the beam–wave coupling performance, and Q_e and Q_0 are the external quality factor and the intrinsic quality factor, respectively [22], [23], [24]. Fig. 7 shows the electric field distributions of three types of cavities. Compared with the traditional interaction circuit, such highly overmoded systems support an

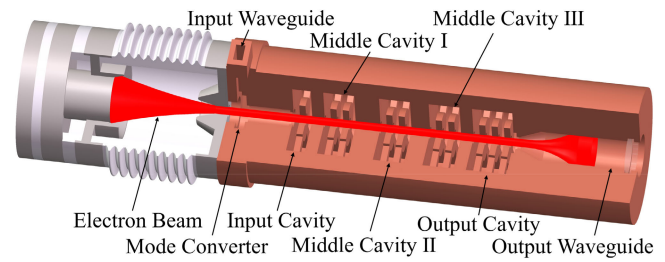


Fig. 6. Schematic of a five-cavity *Ka*-band EIK.

TABLE I
PARAMETERS OF EACH CAVITY

Cavity	f (GHz)	p (mm)	$M^2(R/Q)$ (Ω)	Q_e	Q_0
Input Cavity	32.88	3.85	5.6	443	4128
Middle Cavity I	32.87	3.85	9.8		3999
Middle Cavity II	32.91	3.83	9.7		3954
Middle Cavity III	32.95	3.80	9.6		3911
Output Cavity	32.89	3.70	14.4	663	4831

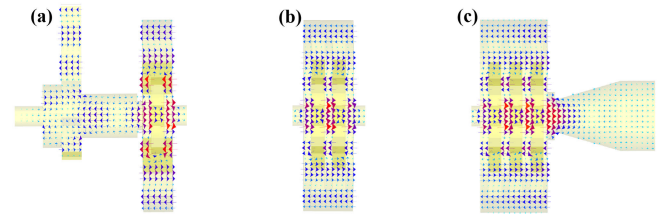


Fig. 7. Simulated electric field distribution on the longitudinal section of (a) input cavity, (b) middle cavity, and (c) output cavity.

axial electric field that is strongest on and near the central axis of the cavity, thereby enhancing the ability to interact with the electron beam passing through the central axis. Another important advantage is that the maximum axial field energy of the quasi- TM_{04} mode can also be easily coupled directly to the output waveguide through conventional aperture diffraction.

This coupling method belongs to the basic form of electrical coupling of aperture coupling, which can be explained by the classic small aperture diffraction theory [19]. The condition for coupling between the main and secondary resonators or waveguides through the small aperture is that the normal component of the electric field or the tangential component of the magnetic field in the same direction exists in the main and secondary resonators or waveguides at the same time, and these components cannot be zero at the same time at the position of the small aperture. Since the TM_{04} -based mode has a normal electric field perpendicular to the common wall, through a small hole opened on the central axis of the end of the cavity, the electric field lines will pass through the small hole and excite the TM_{01} mode field in the output waveguide to propagate, as shown in Fig. 7(c). Compared with the traditional rectangular waveguide TE_{10} mode output, the circular waveguide TM_{01} has a larger power capacity as a high-order mode. Moreover, a larger output port can usually be designed through the output of the circular waveguide TM_{01} mode, which will facilitate the processing and welding of the output window.

TABLE II
PARAMETERS RELATED TO MODE INTERVALS
IN DIFFERENT GAP NUMBERS

Number of Gaps (N)	Δf_1 (GHz)	Δf_2 (GHz)	Δf_3 (GHz)	$M^2(R/Q)_1$ (Ω)	$M^2(R/Q)_2$ (Ω)	$M^2(R/Q)_3$ (Ω)
2	2.29	8.12	9.12	0.12	2.68	3.49
3	2.33	2.35	7.19	0.43	0.28	5.75
4	0.80	0.82	1.42	0.13	0.87	0.17

B. Stability Analysis

The designed highly overmoded structure provides a significant step toward solving the size and power constraints of the device, but multimode coexistence and mode competition are naturally enhanced in more oversized HF structures. The established beam–wave interaction theory shows that the electron beam interacts with the E_z component of the electric field in the central region. Therefore, TM_{0n} modes preferably interact with the electron beam on the central axis, where the index n is determined by the variation in the distribution pattern of the axial electric field along the radial direction. The synchronization relationship between the electron beam and the mode field can be expressed as

$$\beta_e p = m\pi \quad (1)$$

$$\beta_e = 2\pi f / v_e \quad (2)$$

$$v_e = c \cdot \sqrt{1 - 1 / \left(1 + \frac{U}{511}\right)^2} \quad (3)$$

where β_e is the propagation constant of the electron beam, v_e is the electron velocity, c is the speed of light, and U is the electron beam voltage. The determination of the electron velocity relies on making the propagation time between the adjacent gaps equal to the period of the electromagnetic wave supported by the resonant circuit to ensure preliminary effective beam–wave interaction. Since the designed circuit is based on a finite period structure realized in a disk-loaded coupled cavity, a number of discrete frequencies are generated by the number of half-wavelengths between the cavity end walls. Typically, the greater the number of periods contained in each cavity, the more discrete modes there will be.

In an oversized cavity, multimode coexistence is naturally enhanced. Due to the dependence of the resonant frequency on the size of the cavity structure, discrete modes close to the frequency of the operating mode should be initially considered. Table II lists the relevant parameters of the main discrete modes with frequencies close to the operating mode. $\Delta f_1 - \Delta f_3$ are three mode intervals, which are successively close to the operating mode frequency. $M^2(R/Q)_1$, $M^2(R/Q)_2$, and $M^2(R/Q)_3$ are the effective characteristic impedances of the corresponding modes, which characterize the beam–wave coupling performance. The product $M^2(R/Q)$ is considered to be positively correlated with the proactive interaction between the electron beam and the mode field. As shown in Table II, modes close to the operating frequency do not necessarily have higher beam–wave coupling capabilities because the beam–wave coupling strength is not only related to the mode field but also to the specific beam voltage.

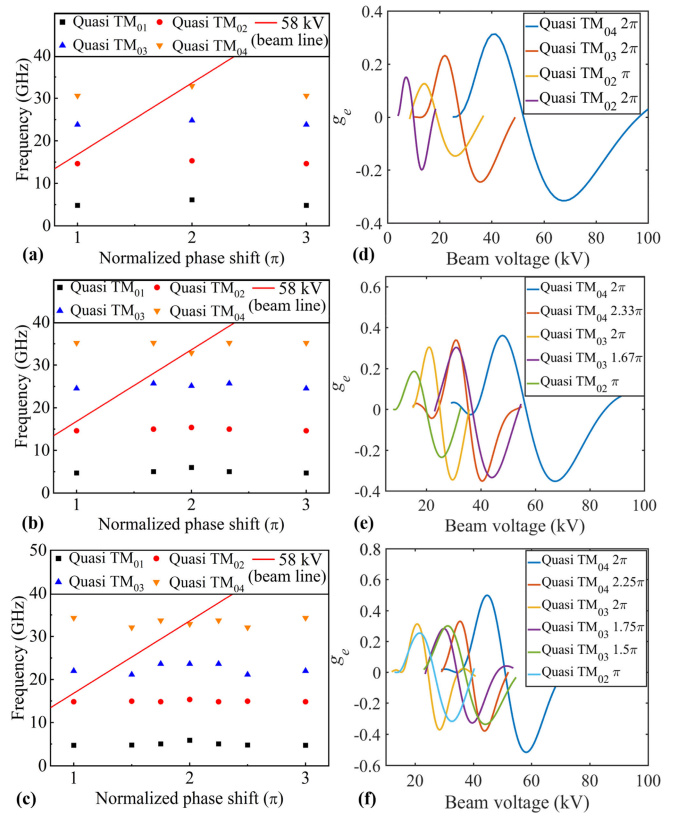


Fig. 8. Dispersion diagrams of (a) two-gap cavity, (b) three-gap cavity, and (c) four-gap cavity. Variation of normalized g_e with the electron beam voltage in (d) two-gap cavity, (e) three-gap cavity, and (f) four-gap cavity.

Generally, the dispersion characteristics of the circuit have the effect of initially reflecting the synchronous conditions of the modes and the beam voltage. Fig. 8(a)–(c) shows the dispersion characteristics of the three structures, which also contains the relevant parameters of the mode interval in Table II. For such multigap interaction cavities formed by periodic slow wave structures (SWSs), the continuous dispersion relation of typical SWS is transformed into a discrete version composed of axial modes. By using the phase shift between adjacent gaps to characterize the discrete axial modes, this also describes the axial electric field distribution of the operating modes in the cavity, such as 2.33π mode and 2π mode. As for $TM_{04} 2\pi$, that is, each gap in the operation mode of TM_{04} has the same direction of the electric field. The discrete modes in the vicinity of the intersection with the beam voltage line are considered to pose a competitive risk to the operating mode. Here, we carry out an extensive study on the beam–wave synchronization and oscillating starting conditions of the designed circuit so as to further suppress possible mode competition. Generally, g_e is used to represent the ability to transfer energy from the electron beam to the circuit, where $g_e = G_e/G_0$. G_e is the beam-load conductance derived from the space-charge wave theory, expressed as [25], [26], [27]

$$G_e = \frac{1}{8} \frac{\beta_e}{\beta_q} G_0 [|M_-^2(\beta_e - \beta_q)| - |M_+^2(\beta_e + \beta_q)|] \quad (4)$$

where β_q is the propagation constants of the reduced plasma and G_0 is the dc conductance of the electron beam.

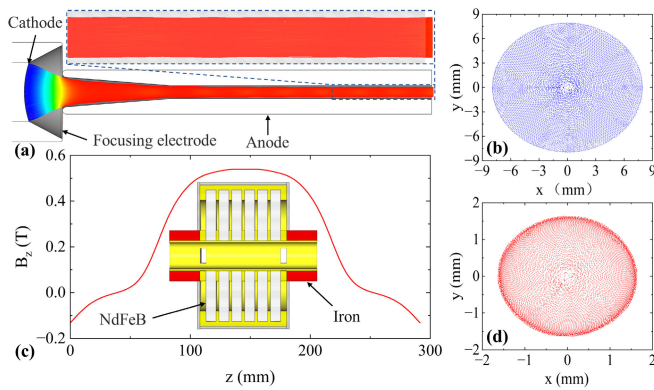


Fig. 9. Electron optical system preliminary design model. (a) Beam trajectory in the electron gun. (b) Size of the electron beam spot on the cathode surface. (c) Magnetic field intensity distribution on the axis of the uniform permanent magnet focusing system. Inset: cross-sectional view of the uniform permanent magnet focusing system. (d) Cross-sectional size of the electron beam within the drift tube.

$M_-(\beta_e - \beta_q)$ and $M_+(\beta_e + \beta_q)$ represent the coupling coefficients of fast and slow space-charge waves, respectively, as follows:

$$M_{\pm}(\beta_e \pm \beta_q) = \frac{\int_{-\infty}^{\infty} E(z)e^{j(\beta_e \pm \beta_q)z} dz}{\int_{-\infty}^{\infty} |E(z)| dz} \quad (5)$$

where $E(z)$ is the axial electric field distribution at the interaction gaps. Negative g_e indicates that the dc energy of the electron beam is converted into HF field energy, and this mode may be excited. Fig. 8(d)–(f) shows the change of g_e with the electron beam dc voltage for the three structures. Through the same calculation and analysis method as in [28], the calculated start-oscillation current I_{st} of all cavities should exceed 22 A within the set larger working range of 55–58 kV. Therefore, the stable operation of quasi-TM₀₄ mode can be guaranteed without self-oscillation.

C. Electron Optical System

Driven by the desire to increase the beam current, extensive research on sheet beam and multibeam has largely provided valuable contributions to overcoming output power limitations [29], [30], [31], [32], [33], [34], [35]. However, the engineering of the focusing system has been challenged due to the difficulty of beam compression and transmission. Since this EIK only requires single-beam operation and has an oversized beam tunnel, a conventional Pierce electron gun can be used to drive this highly overmoded circuit, and a uniform permanent magnet system can be used to maintain the focus of the electron beam [9]. Here, a thermionic electron optical system with a typical structure is designed. Fig. 9(a) shows the trajectory of the electron beam in the entire electron gun cross section. In the preliminary design scheme of the electron gun, electrons are emitted thermally through a heated filament. These emitted electrons are compressed into a usable electron beam under the action of electrostatic field and focusing magnetic field and enter the beam tunnel under the acceleration of the anode.

Through careful engineering of the electron optical system, a uniform electron beam with a maximum envelope diameter

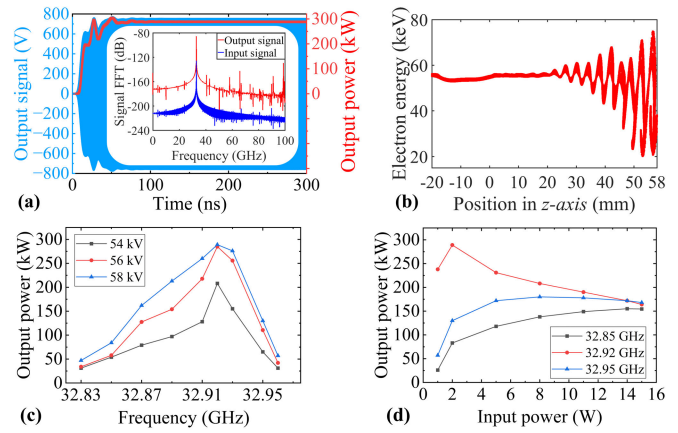


Fig. 10. (a) Output signal power. Inset: frequency spectrums of the input and output signals. (b) Phase-space diagram of electron energy. (c) Output power as a function of input signal sweep frequency characteristics. (d) Output power as a function of input power.

of 3.3 mm and a current of 18 A is obtained at a bias of 58 kV. The electron beam cross section is compressed from the cathode emission area of 64.88π mm² into a beam spot of approximately 2.72π mm². Fig. 9(b) and (d) shows the size of the electron beam spot on the cathode emission surface and the cross-sectional size of the electron beam within the drift tube, respectively. The cathode current emission density of the designed electron gun is about 8.84 A/cm². A comparatively uniform electron beam with an area compression ratio of about 23.85 times is obtained. The scheme of the uniform permanent magnet focusing system is shown in the inset of Fig. 9(c). The magnetic system is mainly composed of six NdFeB magnetic rings and iron pole shoes. The maximum magnetic on-axis field strength exceeds 0.5 T. The uniform transmission distance of the electron beam can be guaranteed to exceed 78 mm. A single magnetic ring has an outer diameter of 260 mm, an inner diameter of 60 mm, and a thickness of 20 mm. The remanent flux density of the magnetic ring is 1.47 T.

III. CIRCUIT PERFORMANCE EVALUATION

To further verify the stability and beam–wave interaction capability of the highly overmoded circuit, 3-D particle-in-cell (PIC) simulations are carried out for the HF circuit by using the CST. According to the designed electron optical system scheme, an electron beam with a diameter of 3.3 mm and a current of 18 A is injected into the HF circuit at a bias of 58 kV. To get closer to reality, we use reduced effective conductivity values to replace the extra ohmic losses caused by surface roughness. The correlation effect between rough surface finish and effective conductivity has been presented by Datta et al. [36] and Kirley et al. [37] in their study of conductivity loss analysis of structures. The conductivity of the cavity wall is set to 3.6×10^7 S/m, corresponding to a surface roughness of 0.15 μ m, which is about 62% of the ideal conductivity of oxygen-free copper. Fig. 10(a) shows the output signal, output power, and spectrum when the input power is 2 W at 32.92 GHz. A maximum output power of 289 kW is obtained at 32.92 GHz in the circular waveguide TM₀₁ mode, with a corresponding gain and efficiency

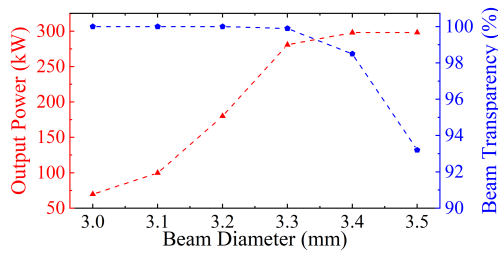


Fig. 11. Output power and beam transparency as a function of beam diameter.

of 51.6 dB and 27.7%, respectively. Fig. 10(b) shows the modulation and bunching when the electron beam interacts with the operating mode. Fig. 10(c) shows the output power as a function of the input signal sweep–frequency characteristics when the input power is 2 W. Fig. 10(d) shows the effect of input power on output performance. The closer to the edge of the operating band, the more power is required to drive this EIK into saturation.

The breakdown electric field threshold for vacuum conditions is given by the Kilpatrick criterion [38]

$$f = 1.6E_{\text{threshold}}^2 \exp(-8.5/E_{\text{threshold}}^2) \quad (6)$$

where f is the RF frequency in the cavity in MHz and $E_{\text{threshold}}$ is the breakdown electric field threshold in MV/m. The “probe” function could be used to monitor the field information in the output cavity. The maximum field strength of the cavity is 15.5 MV/m, which is less than the vacuum breakdown field strength (145 MV/m).

By adjusting the electron gun parameters, the effect of the beam filling rate reflected by the beam diameter on output power and beam transparency is investigated. Fig. 11 shows the output power and beam transparency as a function of beam diameter. The small-ripple electron beam with a diameter of 3.3 mm still has a beam transparency higher than 99.9% when the device works stably and maintains an output power of 289 kW. Therefore, we consider it the best design parameter to make the device operate stably with relatively considerable output power. Considering the subsequent whole tube experiment, we may also adjust the diameter of the electron beam again to ensure the stable operation of the device within the tolerance range.

Based on our experimental basis and operating conditions, the EIK is preliminarily assumed to operate in pulse mode. When we set the pulsewidth of the power supply to be 20 μs and the repetition frequency to be 50 Hz, the duty cycle is 1/1000. When the peak power is 289 kW, the average output power is 289 W. The total average power of the electron beam is 1.044 kW. According to the simulation results shown in Fig. 11, when considering the worst case interception rate of 7%, the power caused by electron interception heating is about 73.1 W. In the tube, the body, the magnets, the output window, and the collector are cooled by the forced flow water. In the worst estimate, referring to the analysis results in [10], the electronic interception power of 73.1 W can be effectively taken away by the cooling water without causing damage to the HF structure. The averaged ohmic loss in the output cavity

can be evaluated, from the relation $\bar{P}_{\text{ohm}} = (Q_e/Q_0) \times \bar{P}_{\text{out}}$, as 39.7 W. By arranging a considerable scale of water-cooling devices around the tube wall, the problem of heat generation can be effectively solved.

IV. CONCLUSION

The substantial increase in the output power of conventional linear beam devices has proven a significant and ongoing technical challenge. Compared with the promising multibeam and sheet-beam structures, here, a highly overmoded structure with the ability to load a high-current single electron beam is designed. Measured S -parameters imply that this highly overmoded structure has the potential for developing high-gain standing-wave amplifiers and broadband traveling-wave amplifiers. A hundred-kilowatt-class Ka -Band EIK based on a quasi- TM_{04} mode RSWS has been verified. These findings highlight that the overmoded operation by increasing circuit size has more potential technical extensions related to the energy conversion of intense beam and wave.

REFERENCES

- [1] D. K. Abe et al., “Millimeter-wave and sub-millimeter-wave vacuum electronics amplifier development at the U.S. naval research laboratory,” *Proc. SPIE*, vol. 8624, Mar. 2013, Art. no. 86240H, doi: 10.1117/12.2012060.
- [2] Y. Gong et al., “Some advances in theory and experiment of high-frequency vacuum electron devices in China,” *IEEE Trans. Plasma Sci.*, vol. 47, no. 5, pp. 1971–1990, May 2019, doi: 10.1109/TPS.2019.2904124.
- [3] J. H. Booske, “Plasma physics and related challenges of millimeter-wave-to-terahertz and high power microwave generation,” *Phys. Plasmas*, vol. 15, no. 5, pp. 1–10, May 2008, doi: 10.1063/1.2838240.
- [4] B. Steer, A. Roitman, P. Horoyski, M. Hyttinen, R. Dobbs, and D. Berry, “High power millimeter-wave extended interaction klystrons for ground, airborne and space radars,” in *Proc. IEEE Radar Conf.*, Oct. 2009, pp. 1–3, doi: 10.1109/RADAR.2009.4976942.
- [5] D. Berry et al., “Practical aspects of EIK technology,” *IEEE Trans. Electron Devices*, vol. 61, no. 6, pp. 1830–1835, Jun. 2014, doi: 10.1109/TED.2014.2302741.
- [6] Z. Chang, G. Shu, Y. Tian, and W. He, “A broadband extended interaction klystron based on multimode operation,” *IEEE Trans. Electron Devices*, vol. 69, no. 2, pp. 802–807, Feb. 2022, doi: 10.1109/TED.2021.3136829.
- [7] N. Guo et al., “Study of a 0.34-THz ladder-type extended interaction klystron with narrow coupling cavities,” *IEEE Trans. Electron Devices*, vol. 68, no. 11, pp. 5851–5857, Nov. 2021, doi: 10.1109/TED.2021.3114392.
- [8] N. Guo et al., “Overlapping-mode extended interaction klystrons for broadband terahertz power amplifiers,” *IEEE Trans. Electron Devices*, vol. 69, no. 3, pp. 1486–1491, Mar. 2022, doi: 10.1109/TED.2022.3147438.
- [9] A. S. Gilmour and I. Ebrary, *Klystrons, Traveling Wave Tubes, Magnetrons, Crossed-Field Amplifiers, and Gyrotrons*. Norwood, MA, USA: Artech House Books, 2011.
- [10] D. Zhao, W. Gu, X. Hou, G. Liu, Q. Xue, and Z. Zhang, “Demonstration of a high-power Ka -band extended interaction klystron,” *IEEE Trans. Electron Devices*, vol. 67, no. 9, pp. 3788–3794, Sep. 2020, doi: 10.1109/TED.2020.3008881.
- [11] J. H. Booske et al., “Vacuum electronic high power terahertz sources,” *IEEE Trans. THz Sci. Technol.*, vol. 1, no. 1, pp. 54–75, Sep. 2011, doi: 10.1109/TTHZ.2011.2151610.
- [12] R. K. Parker, R. H. Abrams, B. G. Danly, and B. Levush, “Vacuum electronics,” *IEEE Trans. Microw. Theory Techn.*, vol. 50, no. 3, pp. 835–845, Mar. 2002, doi: 10.1109/22.989967.
- [13] H. Gong, Y. Gong, T. Tang, J. Xu, and W.-X. Wang, “Experimental investigation of a high-power Ka -band folded waveguide traveling-wave tube,” *IEEE Trans. Electron Devices*, vol. 58, no. 7, pp. 2159–2163, Jul. 2011, doi: 10.1109/TED.2011.2148119.

- [14] C. Paoloni, M. Mineo, M. Henry, and P. G. Huggard, "Double corrugated waveguide for Ka-band traveling wave tube," *IEEE Trans. Electron Devices*, vol. 62, no. 11, pp. 3851–3856, Nov. 2015, doi: [10.1109/TED.2015.2480535](https://doi.org/10.1109/TED.2015.2480535).
- [15] D. Wang, G. Wang, J. Wang, S. Li, P. Zeng, and Y. Teng, "A high-order mode extended interaction klystron at 0.34 THz," *Phys. Plasmas*, vol. 24, no. 2, pp. 1–12, Feb. 2017, doi: [10.1063/1.4975649](https://doi.org/10.1063/1.4975649).
- [16] S. Lü, C. Zhang, S. Wang, and Y. Wang, "Stability analysis of a planar multiple-beam circuit for W-band high-power extended-interaction klystron," *IEEE Trans. Electron Devices*, vol. 62, no. 9, pp. 3042–3048, Sep. 2015, doi: [10.1109/TED.2015.2435031](https://doi.org/10.1109/TED.2015.2435031).
- [17] X. Li et al., "High-efficiency study of an SBEIO based on the SAA optimization," *IEEE Trans. Electron Devices*, vol. 66, no. 11, pp. 4938–4942, Nov. 2019, doi: [10.1109/TED.2019.2941147](https://doi.org/10.1109/TED.2019.2941147).
- [18] X. Zhang, R. Zhang, and Y. Wang, "Study of a dual-mode multibeam interaction circuit with coaxial structure for Ka-band high-power EIK," *IEEE Trans. Electron Devices*, vol. 68, no. 2, pp. 822–828, Feb. 2021, doi: [10.1109/TED.2020.3044553](https://doi.org/10.1109/TED.2020.3044553).
- [19] D. M. Pozar, *Microwave Engineering*, 4th ed. New York, NY, USA: Wiley, 2011.
- [20] C. L. Kory, M. E. Read, R. L. Ives, J. H. Booske, and P. Borchard, "Design of overmoded interaction circuit for 1-kW 95-GHz TWT," *IEEE Trans. Electron Devices*, vol. 56, no. 5, pp. 713–720, May 2009, doi: [10.1109/TED.2009.2015405](https://doi.org/10.1109/TED.2009.2015405).
- [21] Q. Chen et al., "Development of a Ka-band circular TM_{01} to rectangular TE_{10} mode converter," *IEEE Trans. Electron Devices*, vol. 67, no. 3, pp. 1254–1258, Mar. 2020, doi: [10.1109/TED.2020.2968347](https://doi.org/10.1109/TED.2020.2968347).
- [22] X. Xu et al., "Design of a G-band extended interaction klystron based on a three-coupling-hole structure," *IEEE Trans. Electron Devices*, vol. 69, no. 3, pp. 1368–1373, Mar. 2022, doi: [10.1109/TED.2021.3138840](https://doi.org/10.1109/TED.2021.3138840).
- [23] Y. Ding, *Theory and Computer Simulation of High Power Klystron*. Beijing, China: National Defense Industry Press, 2008, pp. 44–47.
- [24] N. Guo et al., "Analysis and improvement of performance instability in extended interaction klystrons with random geometrical perturbations," *IEEE Trans. Electron Devices*, vol. 69, no. 10, pp. 5886–5894, Oct. 2022, doi: [10.1109/TED.2022.3200631](https://doi.org/10.1109/TED.2022.3200631).
- [25] M. Chodorow and T. Wessel-Berg, "A high-efficiency klystron with distributed interaction," *IRE Trans. Electron Devices*, vol. 8, no. 1, pp. 44–55, Jan. 1961, doi: [10.1109/T-ED.1961.14708](https://doi.org/10.1109/T-ED.1961.14708).
- [26] D. H. Preist and W. J. Leidigh, "Experiments with high-power CW Klystrons using extended interaction catchers," *IEEE Trans. Electron Devices*, vol. ED-10, no. 3, pp. 201–211, May 1963.
- [27] X. Zhang, R. Zhang, and Y. Wang, "Research on a high-order mode multibeam extended-interaction oscillator with coaxial structure," *IEEE Trans. Plasma Sci.*, vol. 48, no. 6, pp. 1902–1909, Jun. 2020, doi: [10.1109/TPS.2020.2987042](https://doi.org/10.1109/TPS.2020.2987042).
- [28] L. Bi et al., "Design and analysis of a high-order mode ladder-type RF circuit for stable operation in a W-band extended interaction oscillator," *IEEE Trans. Electron Devices*, vol. 66, no. 1, pp. 729–735, Jan. 2019, doi: [10.1109/TED.2018.2882956](https://doi.org/10.1109/TED.2018.2882956).
- [29] J. Pasour et al., "Demonstration of a 100-kW solenoidally focused sheet electron beam for millimeter-wave amplifiers," *IEEE Trans. Electron Devices*, vol. 58, no. 6, pp. 1792–1797, Jun. 2011, doi: [10.1109/TED.2011.2126577](https://doi.org/10.1109/TED.2011.2126577).
- [30] N. M. Ryskin et al., "Planar microstrip slow-wave structure for low-voltage V-band traveling-wave tube with a sheet electron beam," *IEEE Electron Device Lett.*, vol. 39, no. 5, pp. 757–760, May 2018, doi: [10.1109/LED.2018.2821770](https://doi.org/10.1109/LED.2018.2821770).
- [31] G. V. Torgashov, R. A. Torgashov, V. N. Titov, A. G. Rozhnev, and N. M. Ryskin, "Meander-line slow-wave structure for high-power millimeter-band traveling-wave tubes with multiple sheet electron beam," *IEEE Electron Device Lett.*, vol. 40, no. 12, pp. 1980–1983, Dec. 2019, doi: [10.1109/LED.2019.2945502](https://doi.org/10.1109/LED.2019.2945502).
- [32] N. Kumar et al., "Pseudospark-driven high-current miniaturized voltage-tunable sheet-electron-beam source," *IEEE Trans. Electron Devices*, vol. 68, no. 12, pp. 6482–6486, Dec. 2021, doi: [10.1109/TED.2021.3119555](https://doi.org/10.1109/TED.2021.3119555).
- [33] E. A. Gelvich, L. M. Borisov, Y. V. Zhary, A. D. Zakurdayev, A. S. Pobedonostsev, and V. I. Poognin, "The new generation of high-power multiple-beam klystrons," *IEEE Trans. Microw. Theory Techn.*, vol. 41, no. 1, pp. 15–19, Jan. 1993, doi: [10.1109/22.210224](https://doi.org/10.1109/22.210224).
- [34] A. Bansiwala, S. Raina, K. J. Vinoy, and S. K. Datta, "A post-loaded rectangular reentrant cavity for broadband multiple-beam klystron," *IEEE Electron Device Lett.*, vol. 41, no. 6, pp. 916–919, Jun. 2020, doi: [10.1109/LED.2020.2989103](https://doi.org/10.1109/LED.2020.2989103).
- [35] F.-M. Lin, S. Wu, Y. Xiao, and L. Zhang, "A 0.3 THz multi-beam extended interaction klystron based on $TM_{10,1,0}$ mode coaxial coupled cavity," *IEEE Access*, vol. 8, pp. 214383–214391, 2020, doi: [10.1109/ACCESS.2020.3040394](https://doi.org/10.1109/ACCESS.2020.3040394).
- [36] S. K. Datta, L. Kumar, and B. N. Basu, "A simple and accurate analysis of conductivity loss in millimeter-wave helical slow-wave structures," *J. Infr., Millim., THz Waves*, vol. 30, no. 4, pp. 381–392, Apr. 2009, doi: [10.1007/s10762-008-9455-5](https://doi.org/10.1007/s10762-008-9455-5).
- [37] M. P. Kirley, N. Carlsson, B. B. Yang, and J. H. Booske, "Study of the effect of surface roughness and skin depth on the conductivity of metals at 650 GHz," in *Proc. IVEC*, Apr. 2012, pp. 239–240, doi: [10.1109/IVEC.2012.6262147](https://doi.org/10.1109/IVEC.2012.6262147).
- [38] W. Peter, R. J. Faehl, A. Kadish, and L. E. Thode, "Criteria for vacuum breakdown in RF cavities," *IEEE Trans. Nucl. Sci.*, vol. NS-30, no. 4, pp. 3454–3456, Aug. 1983, doi: [10.1109/TNS.1983.4336689](https://doi.org/10.1109/TNS.1983.4336689).